Analyzing the filamentation of MeV-range proton bunches in a laser-driven ion beamline and optimizing their peak intensity

M. Metternich[☉],[1] H. Nazary[☉],[1] D. Schumacher[☉],[2] C. Brabetz[☉],[2] F. Kroll[☉],[3,4] F.-E. Brack[☉],[3,4] M. Ehret[☉],[1,5] A. Blažević[☉],[2,6] U. Schramm[☉],[3,4] V. Bagnoud[☉],[1,2,6] and M. Roth[☉][1]

[1]*Institut für Kernphysik, Technische Universität Darmstadt, D-64289 Darmstadt, Germany*
[2]*GSI Helmholtzzentrum für Schwerionenforschung, D-64291 Darmstadt, Germany*
[3]*Helmholtz-Zentrum Dresden—Rossendorf, D-01328 Dresden, Germany*
[4]*Technische Universität Dresden, D-01062 Dresden, Germany*
[5]*University of Bordeaux, CNRS, CEA, CELIA (Centre Lasers Intenses et Applications), F-33405 Talence, France*
[6]*Helmholtz-Institut Jena, D-07734 Jena, Germany*

In this article, we report on the latest investigations and achievements in proton beam shaping with our laser-driven ion beamline at GSI Helmholtzzentrum für Schwerionenforschung GmbH. This beamline was realized within the framework of the Laser Ion Generation, Handling, and Transport (LIGHT) collaboration to study the combination of laser-driven ion beams with conventional accelerator components. At its current state, the ions are accelerated by the high-power laser PHELIX via target normal sheath acceleration, and two pulsed high-magnetic solenoids are used for energy selection, transport, and transverse focusing. In between the two solenoids, there is a rf cavity that gives the LIGHT beamline the capability to longitudinally manipulate and temporally compress ion bunches to sub-nanosecond durations. To get optimal results, the rf cavity has to be synchronized with the PHELIX laser and therefore a reliable measurement of the temporal ion beam profile is necessary. In the past, these measurements showed unexpected correlations between the temporal beam profile and the phase as well as the electric field strength of the cavity. In this article, we present a numerical simulation of the beam transport through the LIGHT beamline which explains this behavior by a beam filamentation. We also report on our latest experimental campaigns, in which we combined transverse and longitudinal focusing for the first time. This led to proton bunches with a peak intensity of $(3.28 \pm 0.24) \times 10^8$ protons/(ns mm^2) at a central energy of (7.72 ± 0.14) MeV. The intensity refers to a circle with a diameter of (1.38 ± 0.02) mm that encloses 50% of the protons in the focal spot at the end of the beamline. The temporal bunch width at this position was (742 ± 40) ps (FWHM).

I. INTRODUCTION

Laser plasma accelerators are capable to generate intense multi-MeV ion bunches with short durations on a μm-scale [1,2]. The properties of these laser-generated beams therefore fundamentally differ from those of conventional ion sources and thus offer the potential to expand the scope of accelerators for applications and research [3]. This applies in particular for applications in high-energy density physics in which they could be used as a direct driver in inertial confinement fusion [4], for the exploration of warm dense matter [5], as a probing beam in stopping power

experiments, or as a new kind of ion source for conventional accelerators [6,7]. But also in the field of radiation therapy, laser-driven ion accelerators are discussed as an alternative ion source [8,9] since they are able to provide multi-MeV proton and carbon bunches in very short durations and therefore have the potential to further improve the methodology by utilizing the lately discovered ultrahigh dose rate (FLASH) radiotherapy which showed very promising results [9,10]. The most studied and widely used mechanism is the target normal sheath acceleration (TNSA), as it is particularly suitable due to its robustness and the accompanying reliability. However, for a large part of the mentioned applications, the initial TNSA beam is not suitable because of its broad energy spread, its large divergence, and the background radiation environment in form of an electromagnetic pulse, x rays, and electrons near its origin. For this reason, laser-driven beamlines with conventional accelerator elements like quadrupoles,

solenoids, and plasma lenses are used in various laboratories around the world to shape the beam to the respective requirements. In the following, a few selected concepts will be presented briefly: Our collaboration partners from Helmholtz Zentrum Dresden-Rossendorf (HZDR) operated a laser-driven beamline based on pulsed high-field solenoid magnets for beam transport and dose application for small animal radiobiology [11,12]. At the University of Peking (China) and at the Berkeley Lab Laser Accelerator (BELLA) Center, which is part of the Lawrence Berkeley National Laboratory (LBNL), as well as at the ATLAS 300 laser in Garching near Munich, similar goals are being pursued by using quadrupoles, bending magnets or plasma lenses for the beam shaping [13–15]. At ELI beamlines in Prague (Czech), the first open user irradiation beamline with laser plasma–accelerated ion beams (ELIMED-ELIMAIA) is in construction [16] and at the VEGA 2 system in Salamanca (Spain), a very compact beamline with a dipole magnet and a pinhole was realized [17] which generated very short proton bunches with a very low energy spread even though the bunch intensities were significantly lower than in the other concepts mentioned. The Laser Ion Generation, Handling and Transport (LIGHT) collaboration was also founded in this context and a laser-driven beamline was realized at GSI Helmholtzzentrum für Schwerionenforschung GmbH [7]. The main goal of the LIGHT collaboration is to study the combination of laser-driven ion beams with conventional accelerator components and utilize this knowledge to maximize the bunch intensity and thus demonstrate the potential of laser-driven beamlines. Due to the already existing infrastructure at GSI, it is possible to operate a radiofrequency (rf) cavity which gives the LIGHT beamline the, compared to other laser-driven beamlines, unique possibility to manipulate the bunches longitudinally and thus reduce their energy spread or even temporally compress them. These results already led to several publications [7,18]. The LIGHT collaboration also benefits from the expertise on pulsed high-field solenoid magnets of the HZDR. With these solenoids, the capture efficiency and the transverse focusing of the LIGHT beamline have been optimized [19,20]. In an experimental campaign in January 2020, we combined the temporal compression with the transverse focusing for the first time. This led to $(7.29 \pm 0.64) \times 10^8$ protons in a single bunch with a duration of (742 ± 40) ps (FWHM) which corresponds to a beam current of (157 ± 16) mA. In this article, we want to report on this experimental campaign in detail and compare the results with numerical simulations.

II. SETUP AND CHARACTERISTICS OF THE LIGHT BEAMLINE

In the following, the setup of the LIGHT beamline is described (see Fig. 1). The LIGHT beamline is located at the experimental area Z6 at GSI where the PHELIX laser
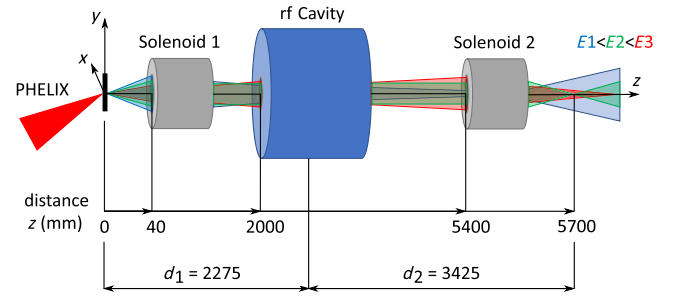
FIG. 1. Schematic illustration of the LIGHT beamline with the most important distances and the coordinate system used in this article.

can be used to accelerate ions via the TNSA mechanism [21]. At the Z6 target chamber, the energy of the PHELIX laser is limited to 30–40 J. With a laser pulse duration of 650 fs and a focal spot size of 3.5 μm (FWHM) on target (typically flat gold or tungsten foils with 5–10 μm thickness), the laser intensity exceeds 10^{19} W/cm^2 which is sufficient to accelerate ions to multi-MeV energies. For protons, the energy spectrum is exponentially decaying and has a maximum energy of up to 28.4 MeV [19]. The maximum divergence of the protons is 30° (half angle) for 5-MeV protons and around 5° (half angle) at the maximum energy of 28 MeV. To capture and transport as many ions as possible through the rest of the LIGHT beamline, a pulsed, high-field solenoid magnet is used. The housing of the solenoid typically has a distance of 40 mm to the TNSA target. The focal length of the solenoid is depending on its magnetic field strength as well as on the momentum and the charge state of the ions. Therefore, the solenoid also functions as a tuneable energy selector since the magnetic field strength can be adjusted by its corresponding pulsed power supply. For protons in the range of (9.8 ± 0.5) MeV, the capture efficiency was determined in [19] to be 34%. The energy distribution of the ion bunch behind the solenoid is Gaussian with an energy spread of around 20% for a peak energy of around 7–10 MeV [19]. Because of this, the temporal width of the bunch is increasing by approximately 1.3 ns per meter (FWHM). For most applications, a narrow energy spread and a short bunch width is advantageous if not necessary. To achieve this, a radio-frequency (rf) cavity is placed behind the first solenoid. It is a three-gap spiral resonator operating at 108.4 MHz and a maximal electrical potential of ±1 MV. Due to the picosecond bunch duration at its origin, the TNSA ions have a strict linear relation between their phase and momentum (low longitudinal emittance) [3]. For this reason, the rf cavity can decrease the energy spread of the bunch to $(2.7 \pm 1.7)\%$ or even temporally compress it to sub-ns durations [7,18]. At the end of the LIGHT beamline, the ion bunch is transversely focused by a second solenoid which is identically constructed to the solenoid at the beginning of the beamline [20]. The most relevant distances

of the described components to the origin of the beamline are shown in Fig. 1.

III. SIMULATION STUDIES ON THE BUNCH FILAMENTATION

In this section, we present our simulation studies on the proton transport through the LIGHT beamline. For an approximately realistic magnetic field of the solenoid magnet, these can reproduce the filamentation of the transverse beam profile (x-y plane) of the transported proton bunches, which has always been present in the experiments with the LIGHT beamline.

This section is divided into three subsections. In Sec. III A, the generation of the TNSA beam in the simulation is explained. After that, the cause of beam filamentation is investigated in Sec. III B by comparing the beam profiles of a TNSA beam transported by solenoids whose magnetic fields were generated with different wire geometries. In Sec. III C, the beam filamentation is then analyzed at the end of the beamline.

A. Reconstruction of a typical TNSA beam at the origin of the beamline

In the simulation, the trajectories of the protons are calculated by solving the Lorentz equation with the MATLAB ordinary differential equation suite [22]. Therefore, the initial position (x, y, z), velocity (v_x, v_y, v_z) and starting time t_0 need to be assigned to each particle. As shown in Fig. 1, the coordinate system is defined so that the z axis corresponds to the nominal trajectory which is always in the center of the beamline. Accordingly, x is the horizontal location deviation and y is the vertical location deviation from the center. First of all, an energy is assigned to each particle. From radiochromic film imaging spectroscopy (RIS) near the origin of the beam it was measured, that the energy distribution dN/dE of the TNSA beam is

$$\frac{dN}{dE} = \frac{N_0}{E} \exp\left(-\frac{E}{k_B T}\right). \tag{1}$$

Such a spectrum is generated with the corresponding cumulative distribution function. Thereby the number of particles can be chosen freely as well as the cutoff energy E_{cut} and the minimum energy E_{min}. After assigning energy to each particle, their corresponding maximum initial divergence θ_{max} is set which relates to the energy as follows:

$$\theta_{\text{max}} = a_2 E^2 + a_1 E + a_0. \tag{2}$$

The parameters $(k_B T, E_{\text{cut}}, a_2, a_1, a_0)$ are determined by fits to the RIS data. In Table I, the values used for the simulations of this article are shown. The minimum energy E_{min} was set to 2 MeV since particles with lower energies are not of interest in this article.

TABLE I. Parameters that were used to generate a TNSA beam in the simulation studies.

$k_B T$	E_{cut}	a_2	a_1	a_0
6 MeV	22 MeV	$-0.04°/\text{MeV}^2$	$0.41°/\text{MeV}$	$26.47°$

To account for the transverse and longitudinal emittance of the initial beam, a random microdivergence $\Delta\theta_{(x,y,z)}$ as well as a random start delay t_0 is added to each particle regardless of its energy. Let $\mathcal{U}_{[a,b]}$ be uniformly distributed random numbers in the interval $[a, b]$ and $\mathcal{N}_{(x,y,z)}(\mu, \sigma^2)$ be normally distributed random numbers with a mean value μ and a standard deviation σ, then

$$\Delta\theta_{(x,y,z)} = \Delta\theta_{\text{max}}\mathcal{N}_{(x,y,z)}(\mu = 0, \sigma^2 = 0.2), \tag{3}$$

with $\Delta\theta_{\text{max}} = 10$ mrad and

$$t_0 = \mathcal{U}^t_{[0,\Delta t_{\text{max}}]}, \tag{4}$$

with $\Delta t_{\text{max}} = 50$ ps. According to [23], this results in an emittance that is in the range of the real emittance of the TNSA beam. Now only the source size r has to be characterized. In [24], a real source size between $r_{\text{min}} = 50$ μm and $r_{\text{max}} = 380$ μm, with a linear dependency on the energy, was determined. These values have been adopted. The beam parameters $(x, y, z, v_x, v_y, v_z, t_0)$ are then determined as follows:

$$\theta = \sqrt{\mathcal{U}^\theta_{[0,\theta_{\text{max}}]}}, \qquad \phi = \mathcal{U}^\phi_{[0,2\pi]}, \tag{5}$$

$$r = (r_{\text{max}} - (r_{\text{max}} - r_{\text{min}}) \cdot E/E_{\text{cut}})\theta/\theta_{\text{max}}, \tag{6}$$

$$\begin{pmatrix} x \\ y \\ z \end{pmatrix} = r \cdot \begin{pmatrix} \cos(\phi) \\ \sin(\phi) \\ 0 \end{pmatrix}, \tag{7}$$

$$v_{\text{total}} = c\sqrt{1 - 1/\gamma^2}, \tag{8}$$

$$\begin{pmatrix} v_x \\ v_y \\ v_z \end{pmatrix} = v_{\text{total}} \cdot \begin{pmatrix} \sin(\theta + \Delta\theta_x) \cdot \cos(\phi) \\ \sin(\theta + \Delta\theta_y) \cdot \sin(\phi) \\ \cos(\theta + \Delta\theta_z) \end{pmatrix}. \tag{9}$$

The number of particles can be chosen freely at the cost of calculation time. The energy spectrum and the correlation between the location deviation x, the direction deviation x', the initial direction deviation r'_0, and the energy E of the generated particles are shown in Fig. 2. As one can see the number of protons is decreasing exponentially to higher energies whereas the corresponding source size and divergence decreases.
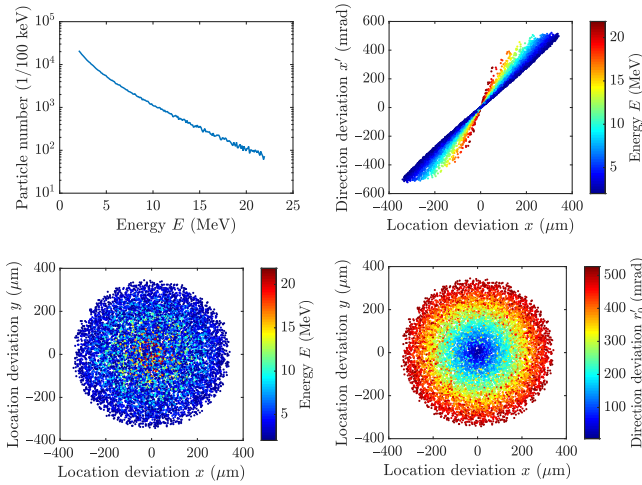
FIG. 2. Energy spectrum and correlation between the location deviation x, the direction deviation x', the initial direction deviation r'_0, and the energy E of a TNSA beam with protons generated by the LIGHT simulation.

B. Investigations in the cause of the beam filamentation

As already mentioned at the beginning of the last subsection, the trajectories of the protons are calculated by numerically solving the Lorentz equation. Since the generated TNSA beam is radially symmetric, it is most likely that the filamentation is caused by an asymmetry in the magnetic field of the solenoid, which in turn can only be caused by its connection cables or the slight inclination of its windings. To investigate this further, the magnetic field of solenoid magnets with different wire geometries is calculated and then the beam profile of the proton bunch is simulated in the middle of the LIGHT beamline for each of these magnetic fields. The following wire geometries are used: (i) radially symmetric ring wires [Figs. 3(a) and 3(b)], (ii) connected helix wires [Figs. 3(c) and 3(d)], (iii) radially symmetric ring wires with straight connection cables [Figs. 3(e) and 3(f)], and (iv) realistic wire geometry [Figs. 3(g) and 3(h)]. All four wire geometries have 100 windings (4×25) with the same radii and also the coil lengths are identical (see Fig. 3). The corresponding magnetic fields of the first three-wire geometries are calculated with MATLAB. Therefore the geometries were approximately reconstructed with many straight line wires. The magnetic field of those is determined using the Biot–Savart law. The sum of all the individual magnetic fields then results in the magnetic field of the solenoid. For the realistic wire geometry, the coil was constructed in a computer-aided design (CAD) software and the corresponding magnetic field was then determined with the COMSOL Multiphysics® software. For both methods, a current of 1A was used to generate a 3D field map with a grid size of 1 mm. In the simulation, the magnetic field strength is then adjusted by multiplying the entire field map by the desired
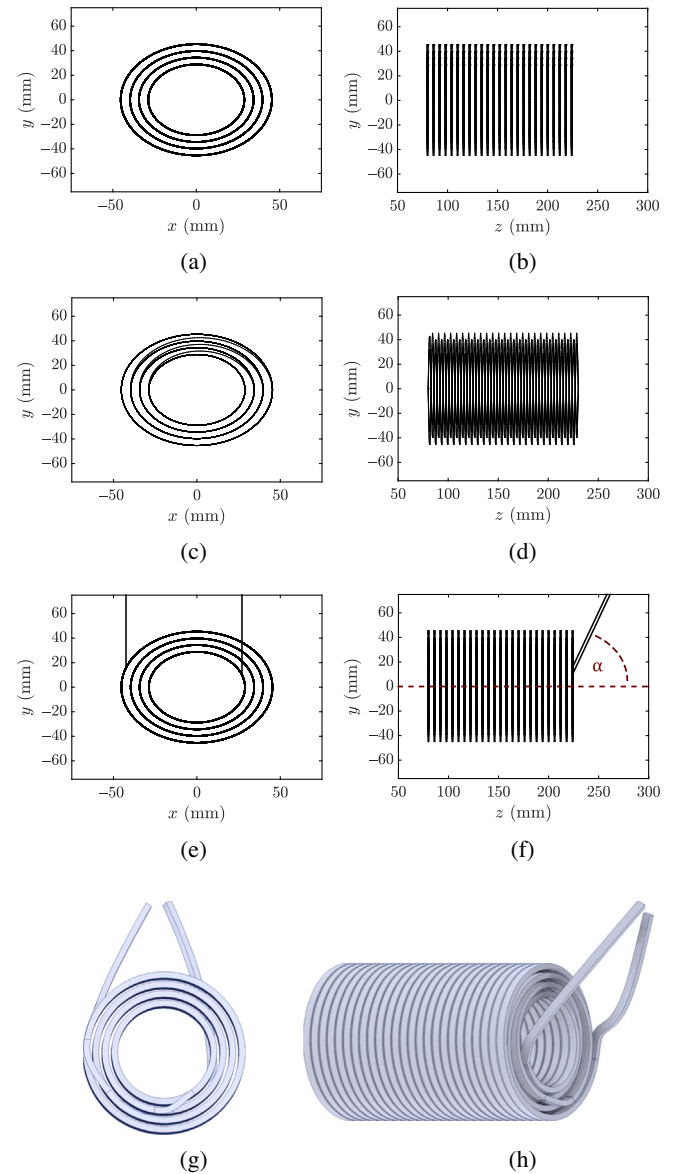
FIG. 3. The different wire geometries of the solenoid magnet that were used in the simulation studies of Sec. III B. (a) Front and (b) side view of the radially symmetric ring wires, (c) front and (d) side view of the connected helix wires, (e) front and (f) side view of the radially symmetric ring wires with connection cables as well as (g) front and (h) side view of the realistic wire geometry.

factor and during the trajectory calculation, the field map is linearly interpolated for the particle positions.

The beam profiles of the transported protons at the center of the LIGHT beamline (2.5 m from its origin) are shown in Fig. 4. Thereby Fig. 4(a) belongs to the radially symmetric ring wires, Fig. 4(b) to the connected helix wires, Fig. 4(c) to the radially symmetric ring wires with straight connection cables, and Fig. 4(d) to the realistic wire geometry. The beam profile shown in Fig. 4(a) is radially symmetric to the z axis which has to be the case since the generated TNSA beam as well as the wire geometry have this
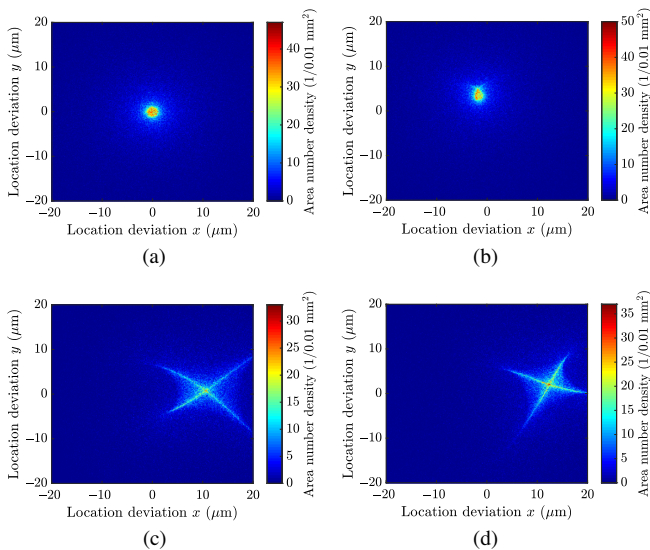
FIG. 4.   Beam profiles of transported protons at the center of the LIGHT beamline (2.5 m from its origin). The deviations of these beam profiles are due to the different magnetic field distributions used in the simulations. (a) Corresponding beam profile to the symmetric ring wires, (b) corresponding beam profile to the connected helix wires, (c) corresponding beam profile to the symmetric ring wires with connection cables ($\alpha = 60°$) and (d) corresponding beam profile to the realistic wire geometry.

symmetry. In the case of the connected helix wires, this symmetry remains for the most part and therefore only slight deviations between Figs. 4(a) and 4(b) can be seen. But by adding the magnetic field generated by the connection cables, this symmetry is harmed. In the case that the cables are directed as in Figs. 3(e) and 3(f) (toward the z and y directions), the generated magnetic field is also mainly directed toward this direction and its strength is decreasing with greater distance from the cables. This has two effects [see also Figs. 4(c) and 4(d)]: (i) an astigmatism arises which causes the filamentation of the proton bunch and (ii) the proton bunch is directed toward the x direction [in the case, the connection cables are directed as in Figs. 3(e) and 3(f)].

Whether the magnetic field generated by the connecting cables is directed more toward the z or y direction depends on how the cables are routed away from the coil. It is mainly directed in the y direction when the cables are parallel and mainly directed in the z direction when they are perpendicular to the coil. Since, in particular, the magnetic field in the y direction adds an asymmetry in the magnetic field of the coil, the influence of the connecting cables is greatest when they run parallel to the z axis (see Appendix A). In a future design of the solenoid magnet, the following approaches could therefore be pursued to minimize the influence of the connecting cables: (i) the connecting cables could be guided vertically away from the coil to minimize the y component of their magnetic field, (ii) the connection cables could be guided

close to each other, possibly even twisted together. Thereby, the magnetic fields of the two connecting cables would cancel each other out, (iii) the number of windings could be increased to decrease the relative magnetic field strength of the connecting cables in relation to the coil, (iv) the distance of the connecting cables to the drift tube of the solenoid could be increased by adding additional layers with windings or by increasing the radii of the layers.

C. Analyzing the filamentation of the proton bunch at the end of the beamline

To analyze the filamentation of the proton bunch at the end of the beamline, the magnetic field generated with the realistic wire geometry [see Figs. 3(g) and 3(h)] is used for both solenoids. The deflection of the proton bunch by the magentic field of the connection cables is thereby compensated by transversely shifting the solenoid by 0.2 mm in the x-direction and 0.8 mm in the y-direction.

In Fig. 5, the particles of the simulated focal spot at the end of the beamline are shown. In the upper picture, the color of the particles corresponds to their energy, while in
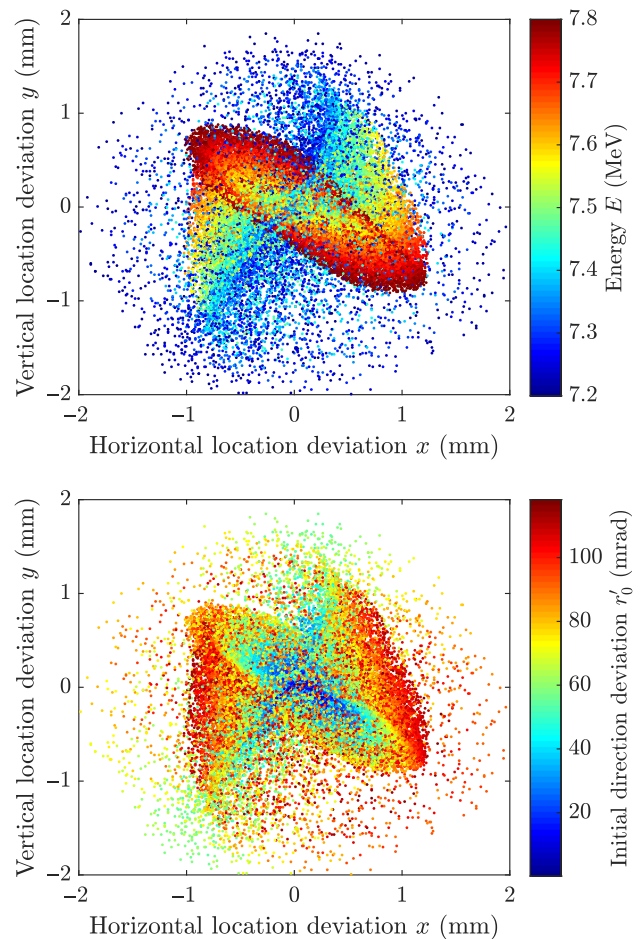
FIG. 5.   The positions of the various protons are shown at the end of the beamline and their energy (upper picture) or their initial direction deviation (lower picture) are indicated by the color.

the lower picture, it corresponds to their initial direction deviation. For each energy, the particle distribution is approximately linear or elliptical in shape and has a different orientation in the *x*-*y* plane. This is due to chromatic aberration and astigmatism of the solenoid magnets. The chromatic aberration is caused by the energy spread of the bunch and the dependency of the focusing strength of the solenoid on the momentum of the respective particle. The astigmatism on the other hand is the consequence of the asymmetry in the magnetic field, which is mainly caused by the connection cables of the solenoid (see. Sec. III B). The distribution of the initial direction deviations of the particles in the lower picture of Fig. 5 reveals a spherical aberration which is due to the great divergence of the beam at its origin. Thus, the entire aperture of the solenoid magnets is used, and the dependency of the focal length of the solenoids on the third-order location deviation [25] is not negligible. To quantify the aberrations of the solenoids, the normalized root mean square (rms) emittance

$$\varepsilon_{n,xx'} = \beta \cdot \gamma \cdot \sqrt{\langle x^2 \rangle \langle x'^2 \rangle - \langle xx' \rangle^2} \qquad (10)$$

of the simulated proton bunch is determined at the end of the beamline. It is 2.41 mm mrad for the *x*-*x'* plane and 2.69 mm mrad for the *y*-*y'* plane.

The energy distribution of the filaments can deviate from the overall energy distribution. This can lead to multipeak structures in the temporal beam profile of the beam if just a fraction of the beam is measured by a detector. This is indicated in Fig. 6 which shows the temporal profiles of the beam fractions enclosed by the green, blue, and red circles. The diameter of the blue and red circles corresponds with 0.5 mm to the size of the detection area of the diamond detector that we typically use in our experimental campaigns [26]. In the experiments, this ultimately leads to an unclear correlation between the shape of the measured temporal beam profile and the phase or the electrical field strength of the cavity. This makes a systematic adjustment of the cavity with a filamented beam unfeasible. Since the adjustment of the cavity is essential to obtain proton bunches with the highest intensities, the suppression of the beam filamentation in the experiment is crucial and will be explained in the next section.

IV. OPTIMIZATION OF THE BUNCH INTENSITY AND SETUP OF THE BEAM DIAGNOSTICS

In this section, we present the experimental procedure used to suppress the beam filamentation and thus optimize the intensity of the proton bunches at the end of the LIGHT beamline.

The first step is the alignment of the first solenoid and the adjustment of its magnetic field strength. We aimed for a central bunch energy of 8 MeV and since the focal length of
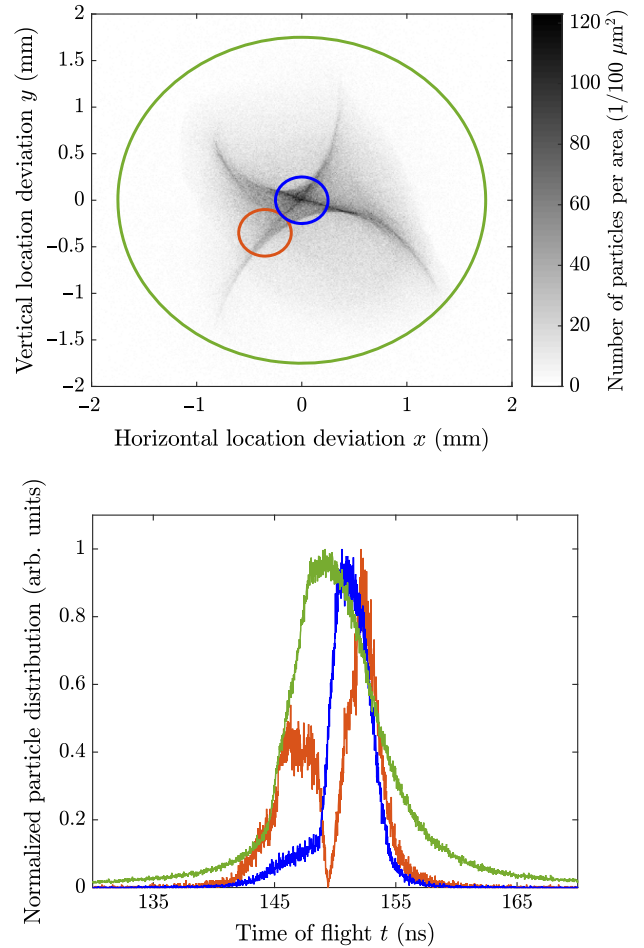
FIG. 6.   In the upper picture, the simulated proton bunch, which was already shown in Fig. 5, is illustrated as a 2D histogram and the temporal profiles of the beam fractions encircled by the green, blue, and red rings are shown in the lower picture.

the solenoid is proportional to the squared momentum of the protons, we had a good estimation for the corresponding settings for the pulsed power supply of the solenoid from the previous experimental campaigns. For the solenoid alignment, the transported beam was diagnosed by radiochromic film imaging spectroscopy (RIS) [23] at the entrances of the rf cavity at first and then at the entrance of the second solenoid. The positioning of the capturing solenoid is done by a hexapod (HXP100-MECAV6) which was installed at the Z6 target chamber in 2019.

The entrance of the second solenoid was 5.4 m behind the TNSA target which means that the bunch is collimated to a good approximation at this point due to the limited apertures of the cavity (35 mm) and the solenoids (40 mm). The alignment and the adjustment of the magnetic field strength of the second solenoid were not as crucial as for the capturing one since the distance from the solenoid to the focal spot was set to just 4 cm. This point was therefore the end of the beamline in the experimental campaign presented here and had a distance of 5.7 m to its origin.

To measure the temporal profile and the energy of the bunch at this position, we used an ultrafast diamond membrane detector [26] and a fast photodiode (rise time < 1 ns). The diamond detector is able to resolve the temporal profile of the beam and was placed directly in the focal spot of the bunch. The photodiode was just slightly displaced to the diamond detector and measured the plasma radiation which is emitted during the interaction between the PHELIX laser and the TNSA target. Since the plasma radiation travels with the speed of light, the time of flight (TOF) of the bunch to the end of the beamline can be determined by the time difference of the rising edge of the photodiode signal and the diamond detector signal.

Some of the first results of these measurements are shown in the upper picture of Fig. 7. The cause of the double and triple peak structures in the temporal profile from shots 21, 29, and 34 can be explained by the
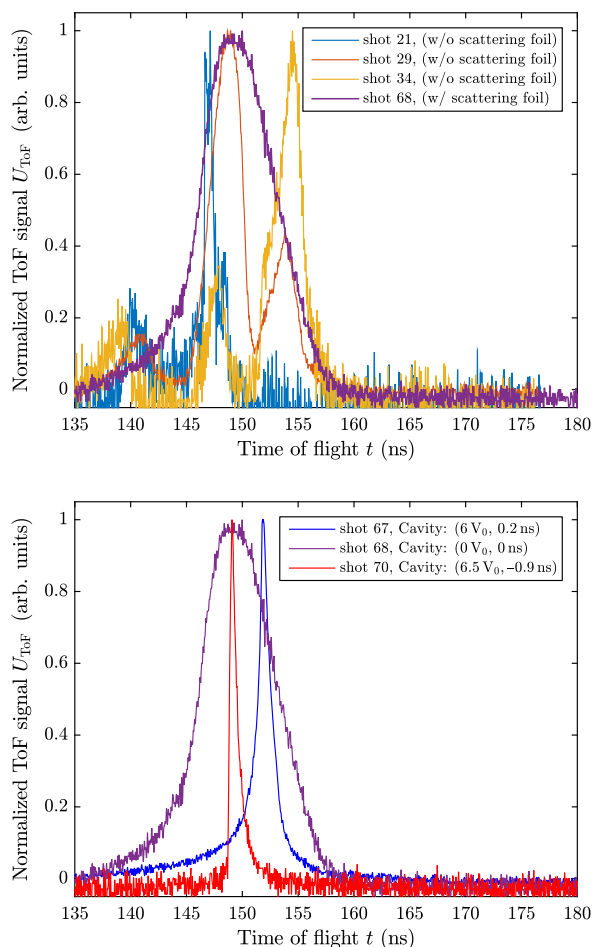
FIG. 7. Measurement of the temporal profile of the proton bunches with an ultrafast diamond detector at the end of the LIGHT beamline. The upper picture shows the results of different shots with and without a scattering foil in front of the second solenoid, whereas the lower picture shows the same measurement (with scattering foil) for different electric field strengths and phases of the cavity.

filamentation of the beam and the small detection area of the diamond detector (0.5 mm) which was already demonstrated in Sec. III. To get the temporal profile of the whole bunch, its filamentation was eliminated by a scattering foil. We used a radiochromic film (RCF) of type Gafchromic HD-V2 (about 100 μm thick) at the entrance of the second solenoid. According to the Stopping and Range of Ions in Matter (SRIM/TRIM) code [27], a mean scattering angle of 0.74° is exhibited by 7.7 MeV protons after passing the RCF which corresponds to a transverse position deviation of 4.53 mm over the distance between the scattering foil and the diamond detector (350 mm). The scattering was sufficient to eliminate the filamentation, as can be seen by the normalized Gaussian distributed TOF signal of shot 68 (purple line), which is enclosing the normalized double and triple peak TOF signals of the shots 21, 29, and 34 in the upper picture of Fig. 7.

Afterward, the rf cavity was set to temporally compress the bunch at the position of the diamond detector which itself was placed in the focal spot of the beam at the end of the beamline as already mentioned. The cavity can approximately be described as an oscillating electrical field in which the protons are accelerated or decelerated depending on their entering time and energy. Since the bunch has already a temporal width of several nanoseconds when entering the cavity, the energy transfer to the individual protons is different. If the cavity is set up so that the fast protons in the front of the bunch are decelerated and the slow protons in the back are accelerated, so the whole bunch is reaching the end of the beamline at the same time, a temporal bunch width in the sub-nanosecond regime can be achieved. The shortest temporal bunch width we measured with the setup described in this section is shown in the lower picture of Fig. 7 (red line) and had an FWHM of (742 ± 40) ps. In [18], the temporal compression of the bunch with the LIGHT beamline is described in more detail and a bunch duration under 500 ps was measured. Nevertheless, in [18], the bunch was not focused on the diamond detector and the filamentation of the beam was not suppressed by a scattering foil. Therefore, the temporal profile measured by the diamond detector in [18] does not represent the temporal profile of the whole bunch.

To measure the focal spot size and the number of particles of the longitudinally and transversely focused proton bunch, the RIS was used once more. Therefore an RCF stack was placed in the focal spot right in front of the diamond detector and the scattering foil in front of the second solenoid was removed. The active layer of the RCF stack in which the longitudinally and transversely focused proton bunch deposited the most amount of energy is illustrated in the upper picture of Fig. 8. To determine the number of protons from the RCF data, a successive deconvolution process was used. This method creates a particle distribution that reproduces the measurement with as few particles as possible. Thereby the only restriction is

Parameter	Value (experiment)
Number of protons	$(7.29 \pm 0.64) \times 10^8$
Peak energy	(7.72 ± 0.14) MeV
Bunch length (FWHM)	(742 ± 40) ps
Focal spot (50% of protons)	(1.38 ± 0.02) mm
Fluence (focal spot)	$(2.44 \pm 0.21) \times 10^8/(\text{mm}^2)$
Intensity (focal spot)	$(3.28 \pm 0.24) \times 10^8/(\text{ns mm}^2)$
Beam current	(157 ± 16) mA

Parameter	Value (simulation)
Energy spread (Appendix B)	5.93%
Normalized emittance (x-x')	2.41 mm · mrad
Normalized emittance (y-y')	2.69 mm · mrad

matches the measured deposited energy in the active layers of the RCF stack, one cannot conclude that this is the energy spectrum of the temporally compressed proton bunch because there are too few data points. Since especially the energy spread of the temporal compressed proton bunch is an important parameter, some further investigations on the energy spectrum can be found in Appendix B.

V. CONCLUSION AND OUTLOOK

In this article, the results of a numerical simulation were shown which has been performed to analyze the filamentation of a laser-driven proton beam in a pulsed high-field solenoid beamline. It revealed that the energy distribution of the filaments can differ significantly from the overall energy distribution of the bunch which can lead to multiple peaks in the temporal beam profile measurement if just a fraction of the bunch is captured by a detector. In an experimental campaign with the LIGHT beamline at GSI, the suppression of the beam filamentation with a scattering foil enabled us to find the best configuration of rf cavity parameters in order to gain the shortest proton bunch durations in the focal spot at the end of the beamline. This led to an intensity of $(3.28 \pm 0.24) \times 10^8$ protons/(ns mm²) with a peak energy of (7.72 ± 0.14) MeV. The intensity refers to a circle with a diameter of (1.38 ± 0.02) mm in the focal spot that contained 50% of the protons and had a bunch width of (742 ± 40) ps (FWHM). The whole bunch therefore had a beam current of (157 ± 16) mA. Meanwhile, the LIGHT collaboration shifted its focus toward performing stopping power experiments with the laser-driven beamline at GSI in order to study the interaction of ions with dense, highly ionized matter [20]. For theory benchmarking, ion bunches with lower velocities (< 1 MeV/u) than normally transported through the beamline are advantageous, since thereby coupling effects between the probing ions and a laser

FIG. 8.　In the upper picture, the deposited energy of the longitudinally and transversely focused proton bunch is shown in the active layer, in which particles with an energy of 7.7 MeV have been stopped. The red circle is enclosing 50% of the total deposited energy in this layer and has a 1.38 mm diameter. In the lower picture, the total measured deposited energy in all the five active layers (red bars) of the stack and a calculated energy spectrum (gray) which would deposit the same energy in these active layers (orange bars) is illustrated. More information on the reconstruction of this energy spectrum is provided in Sec. IV.

that the particle distribution has to be continuous. This is ensured by a linear interpolation between the sample points, which are located at the particle energies that are stopped in the active layers. The spectrum thus obtained is shown in the lower picture of Fig. 8. It contains $(7.29 \pm 0.64) \times 10^8$ protons in total. This value was used to calculate the beam parameters in Table II.

Assuming that most of the protons are getting stopped in the active layer that corresponds to an energy of 7.7 MeV, the number of particles obtained by this method should be a very accurate estimation, especially since the measurements of the temporal bunch profile confirm this assumption. However, it should be mentioned at this point that even though the deposited energy of this spectrum

generated plasma can be achieved and in this regime, the various theories differ most from each other [28]. Therefore, the next goal of the LIGHT collaboration is the generation of intense ions with an energy per mass lower than 1 MeV/u.

APPENDIX A: INFLUENCE OF THE CONNECTION CABLE DIRECTION ON THE BEAM PROFILE

In Sec. III B, it was shown that the filamentation of the proton bunch in the LIGHT beamline is caused by the connection cables of the solenoid magnets. In this appendix, it will be analyzed to which extent the direction in which the connecting cables are led away from the coil has an influence on the beam profile. Therefore, the simulations
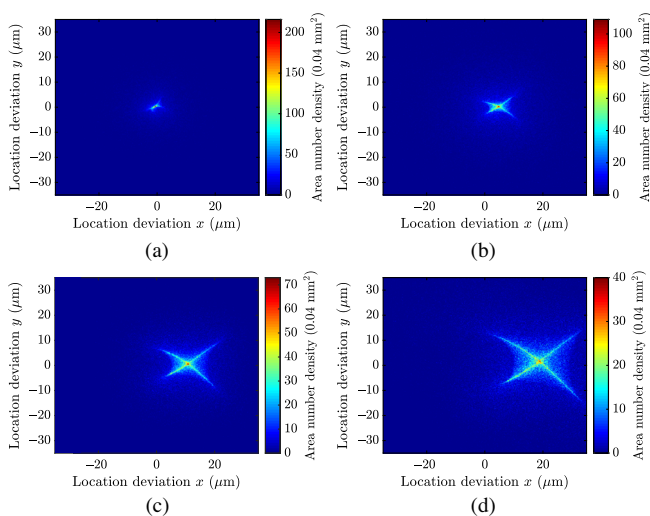
FIG. 9. Beam profiles of transported protons at the center of the LIGHT beamline (2.5 m from its origin). The magnetic field of the solenoid was thereby generated by the wire geometry shown in Figs. 3(e) and 3(f). The deviations of these four beam profiles are due to a different angle α between the x-y plane and the connecting cables. (a) $\alpha = 90°$, (b) $\alpha = 75°$, (c) $\alpha = 60°$, and (d) $\alpha = 45°$.

shown in Sec. III B were performed for a different angle between the x-y plane and the connecting cables [α in Fig. 3(f)]. Otherwise, the wire geometry for calculating the magnetic fields was similar to the one in Figs. 3(e) and 3(f). The results are shown in Fig. 9. As expected, the influence of the connecting cables increases for a smaller angle α since thereby the magnetic field of the connecting cables is directed more toward the y direction and thus increases the asymmetry in the magnetic field of the coil.

APPENDIX B: ENERGY SPECTRUM OF THE TEMPORALLY COMPRESSED PROTON BUNCH

In the following, the energy spread of the temporally compressed proton bunch will be estimated and then compared with a simulation. From the TOF data of shot 68 (see Fig. 7), it can be determined that the energy spread of the uncompressed proton bunch is $\Delta E_{\mathrm{uncomp}}/E = 10.75\%$ (FWHM). The temporal length of the proton bunch in the middle of the cavity is therefore $\Delta t_{\mathrm{cav}} = 2.78$ ns (FWHM). However, it has to be considered that only the fraction of the bunch that passes the cavity in the time in which the change of the electric field is approximately linear ($\approx T_{\mathrm{cav}}/4 = 2.31$ ns) is temporally compressed. Since $T_{\mathrm{cav}}/4 < \Delta t_{\mathrm{cav}}$, only this fraction has to be considered which has a total energy spread of $\Delta E_{\mathrm{linear}}/E = 8.93\%$ before the cavity. The energy spread of this fraction behind the cavity depends on the ratio between the distance from the origin of the beamline to the middle of the cavity (d_1 in Fig. 1) and the distance from the cavity to the point at which the proton bunch shall be temporally compressed (d_2 in Fig. 1). The reason for this is that the change in the temporal length of the bunch depends on its energy spread and the distance it travels. So if, for example, the distance d_1 over which the bunch lengthens in time is twice as long as the distance d_2 over which it contracts, the contraction in time has to be twice as fast to obtain the initial bunch width at the position $d_1 + d_2$. This in turn means that, in this example, the energy spread of the bunch on the distance d_2 has to be twice as large as the energy spread of the bunch on the distance d_1. The energy spread of the temporal compressed fraction of the proton bunch behind the cavity $\Delta E_{\mathrm{comp}}/E$ is therefore approximately:

$$\frac{\Delta E_{\mathrm{comp}}}{E} = \frac{\Delta E_{\mathrm{linear}}}{E}\frac{d_1}{d_2}. \tag{B1}$$

For the experimental setup shown in this article, this results in an energy spread of 5.93 %. Since this is a highly simplified estimation, the value is compared with the result of a simulation in the following. Therefore, the same simulation as shown in Sec. III C was used but the rf cavity was also implemented. As already mentioned in Sec. II, the rf cavity of the LIGHT beamline is a three-gap spiral resonator. The inner gap has a length of 40 mm, the
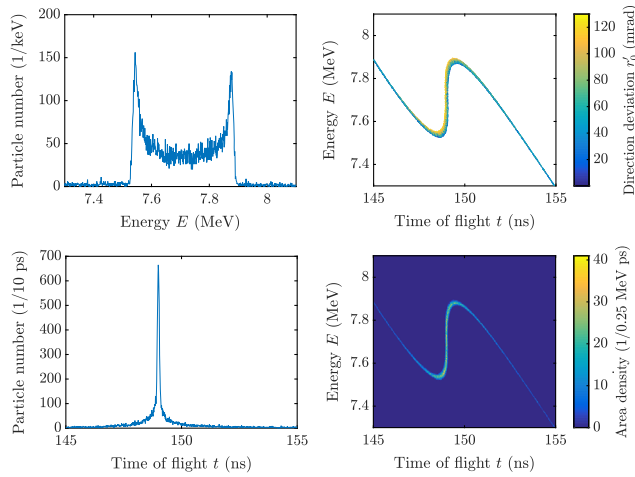
FIG. 10. Energy spectrum, temporal profile, and correlation between the energy E, the time of flight t, and the initial direction deviation r'_0 of the temporally compressed bunch generated by the LIGHT beamline.

outer gaps have a length of 20 mm, and the drift tubes between the gaps have a length of 150 mm. Furthermore, there is a phase shift of 180° between the inner and the outer gaps. In the simulation, the electric field strength is spatially constant in the three gaps and immediately drops to zero in the drift sections. The resulting temporally compressed proton bunch is shown in Fig. 10.

The temporal length of the simulated bunch is only 97 ps (FWHM) since it is only limited by the different distances of the trajectories, which depends mainly on the initial direction deviation r'_0 of the particle. The fact that no proton bunches with such a short temporal length are measured in the experiments is probably due to quenching effects in the diamond detector and space charge effects which are not taken into account in the simulation. The resulting energy spectrum has a u shape with an energy spread of 4.94%. Equation (B1) is therefore suitable for a rough estimation of the resulting energy spread of a temporally compressed proton bunch.

---

[1] A. Macchi, M. Borghesi, and M. Passoni, Ion acceleration by superintense laser-plasma interaction, Rev. Mod. Phys. **85**, 751 (2013).

[2] H. Daido, M. Nishiuchi, and A. S. Pirozhkov, Review of laser-driven ion sources and their applications, Rep. Prog. Phys. **75**, 056401 (2012).

[3] T. E. Cowan *et al.*, Ultralow Emittance, Multi-MeV Proton Beams from a Laser Virtual-Cathode Plasma Accelerator, Phys. Rev. Lett. **92**, 204801 (2004).

[4] M. Roth, T. E. Cowan, M. H. Key, S. P. Hatchett, C. Brown, W. Fountain, J. Johnson, D. M. Pennington, R. A. Snavely, S. C. Wilks, K. Yasuike, H. Ruhl, F. Pegoraro, S. V. Bulanov, E. M. Campbell, M. D. Perry, and H. Powell, Fast Ignition by Intense Laser-Accelerated Proton Beams, Phys. Rev. Lett. **86**, 436 (2001).

[5] P. K. Patel, A. J. Mackinnon, M. H. Key, T. E. Cowan, M. E. Foord, M. Allen, D. F. Price, H. Ruhl, P. T. Springer, and R. Stephens, Isochoric Heating of Solid-Density Matter with an Ultrafast Proton Beam, Phys. Rev. Lett. **91**, 125004 (2003).

[6] P. Antici, M. Migliorati, A. Mostacci, L. Picardi, L. Palumbo, and C. Ronsivalle, A compact post-acceleration scheme for laser-generated protons, Phys. Plasmas **18**, 073103 (2011).

[7] S. Busold, D. Schumacher, O. Deppert, C. Brabetz, F. Kroll, A. Blažević, V. Bagnoud, and M. Roth, Commissioning of a compact laser-based proton beam line for high intensity bunches around 10 MeV, Phys. Rev. ST Accel. Beams **17**, 031302 (2014).

[8] U. Masood, M. Bussmann, T. E. Cowan, W. Enghardt, L. Karsch, F. Kroll, U. Schramm, and J. Pawelke, A compact solution for ion beam therapy with laser accelerated protons, Appl. Phys. B **117**, 41 (2014).

[9] A. Schüller *et al.*, The European Joint Research Project UHDpulse—Metrology for advanced radiotherapy using particle beams with ultra-high pulse dose rates, Phys. Med. **80**, 134 (2020).

[10] J. R. Hughes and J. L. Parsons, FLASH radiotherapy: Current knowledge and future insights using proton-beam therapy, Int. J. Mol. Sci. **21**, 6492 (2020).

[11] F. E. Brack, F. Kroll, L. Gaus, C. Bernert, E. Beyreuther, T. E. Cowan, L. Karsch, S. Kraft, L. A. Kunz-Schughart, E. Lessmann, J. Metzkes-Ng, L. Obst-Huebl, J. Pawelke, M. Rehwald, H. P. Schlenvoigt, U. Schramm, M. Sobiella, E. R. Szabó, T. Ziegler, and K. Zeil, Spectral and spatial shaping of laser-driven proton beams using a pulsed high-field magnet beamline, Sci. Rep. **10**, 9118 (2020).

[12] F. Kroll *et al.*, Tumour irradiation in mice with a laser-accelerated proton beam, Nat. Phys. **18**, 316 (2022).

[13] J. G. Zhu *et al.*, Demonstration of tailored energy deposition in a laser proton accelerator, Phys. Rev. Accel. Beams **23**, 121304 (2020).

[14] L. Obst-Huebl, J. Bin, J.-H. Mao, L. Geulig, H. Chang, K. Nakamura, Q. Ji, J. D. Chant, A. J. Gonsalves, L. He, S. S. Bulanov, C. B. Schroeder, C. G. R. Geddes, B. Simmons, T. Schenkel, E. A. Blakeley, A. M. Snijders, S. Steinke, and E. Esarey, Radiobiological studies with laser-driven protons at the BELLA PW, Proc. SPIE Int. Soc. Opt. Eng. **11790**, 117900B (2021).

[15] T. F. Rösch *et al.*, A feasibility study of zebrafish embryo irradiation with laser-accelerated protons, Rev. Sci. Instrum. **91**, 063303 (2020).

[16] G. A. Cirrone *et al.*, ELIMED-ELIMAIA: The first open user irradiation beamline for laser-plasma-accelerated ion beams, Front. Phys. **8**, 1 (2020).

[17] J. I. Apiñaniz, S. Malko, R. Fedosejevs, W. Cayzac, X. Vaisseau, D. de Luis, G. Gatti, C. McGuffey, M. Bailly-Grandvaux, K. Bhutwala, V. Ospina-Bohorquez, J. Balboa, J. J. Santos, D. Batani, F. Beg, L. Roso, J. A. Perez-Hernandez, and L. Volpe, A quasi-monoenergetic short time duration compact proton source for probing high energy density states of matter, Sci. Rep. **11**, 6881 (2021).

[18] S. Busold, D. Schumacher, C. Brabetz, D. Jahn, F. Kroll, O. Deppert, U. Schramm, T. E. Cowan, A. Blažević, V. Bagnoud, and M. Roth, Towards highest peak intensities

for ultra-short MeV-range ion bunches, Sci. Rep. **5,** 12459 (2015).

[19] S. Busold, D. Schumacher, O. Deppert, C. Brabetz, S. Frydrych, F. Kroll, M. Joost, H. Al-Omari, A. Blažević, B. Zielbauer, I. Hofmann, V. Bagnoud, T. E. Cowan, and M. Roth, Focusing and transport of high-intensity multi-MeV proton bunches from a compact laser-driven source, Phys. Rev. ST Accel. Beams **16,** 101302 (2013).

[20] D. Jahn, D. Schumacher, C. Brabetz, F. Kroll, F. E. Brack, J. Ding, R. Leonhardt, I. Semmler, A. Blažević, U. Schramm, and M. Roth, Focusing of multi-MeV, subnanosecond proton bunches from a laser-driven source, Phys. Rev. Accel. Beams **22,** 011301 (2019).

[21] V. Bagnoud *et al.*, Commissioning and early experiments of the PHELIX facility, Appl. Phys. B **100,** 137 (2010).

[22] L. F. Shampine and M. W. Reichelt, The MATLAB ode suite, SIAM J. Sci. Comput. **18,** 1 (1997).

[23] F. Nürnberg, M. Schollmeier, E. Brambrink, A. Blažević, D. C. Carroll, K. Flippo, D. C. Gautier, M. Geibel, K. Harres, B. M. Hegelich, O. Lundh, K. Markey, P. McKenna, D. Neely, J. Schreiber, and M. Roth, Radiochromic film imaging spectroscopy of laser-accelerated proton beams, Rev. Sci. Instrum. **80,** 033301 (2009).

[24] F. Nürnberg, Laser-accelerated proton beams as a new particle source, Ph.D. thesis, Technische Universität Darmstadt, 2010, https://tuprints.ulb.tu-darmstadt.de/id/eprint/2339.

[25] B. Biswas, A model of field and spherical aberration in soft/hard edge solenoid magnets, Rev. Sci. Instrum. **84,** 103301 (2013).

[26] D. Jahn, M. Träger, M. Kis, C. Brabetz, D. Schumacher, A. Blažević, M. Ciobanu, M. Pomorski, U. Bonnes, S. Busold, F. Kroll, F. E. Brack, U. Schramm, and M. Roth, Chemical-vapor deposited ultra-fast diamond detectors for temporal measurements of ion bunches, Rev. Sci. Instrum. **89,** 093304 (2018).

[27] J. F. Ziegler and J. P. Biersack, The stopping and range of ions in matter, in *Treatise on Heavy-Ion Science: Volume 6: Astrophysics, Chemistry, and Condensed Matter*, edited by D. A. Bromley (Springer, Boston, MA, 1985), pp. 93–129.

[28] W. Cayzac *et al.*, Experimental discrimination of ion stopping models near the Bragg peak in highly ionized matter, Nat. Commun. **8,** 15693 (2017).